Lawrence Berkeley National Laboratory
Recent Work

Title
Composition-Dependent Functionality of Copper Vanadate Photoanodes.

Permalink
https://escholarship.org/uc/item/55r999n3

Journal
ACS applied materials & interfaces, 10(13)

Authors
Jiang, Chang-Ming
Segev, Gideon
Hess, Lucas H
et al.

Publication Date
2018-04-01

Peer reviewed

Composition-Dependent Functionality of Copper Vanadate Photoanodes

Chang-Ming Jiang,[†,‡] Gideon Segev,[†,‡] Lucas H. Hess,[†,‡] Guiji Liu,[†,‡] Gregory Zaborski,[†,‡] Francesca M. Toma,[†,‡] Jason K. Cooper,[†,‡] and Ian D. Sharp*[,§]

[†]Joint Center for Artificial Photosynthesis, [‡]Chemical Sciences Division, Lawrence Berkeley National Laboratory, Berkeley, California 94720, United States

[§]Walter Schottky Institut and Physik Department, Technische Universität München, Am Coulombwall 4, 85748 Garching, Germany

S *Supporting Information*

ABSTRACT: To understand functional roles of constituent elements in ternary metal oxide photoanodes, essential photoelectrochemical (PEC) properties are systematically analyzed on a series of copper vanadate compounds with different Cu:V elemental ratios. Homogeneous and highly continuous thin films of β-$Cu_2V_2O_7$, γ-$Cu_3V_2O_8$, $Cu_{11}V_6O_{26}$, and $Cu_5V_2O_{10}$ are grown via reactive co-sputtering and their performance characteristics for the light-driven oxygen evolution reaction are evaluated. All four compounds have similar bandgaps in the range of 1.83−2.03 eV, though Cu-rich phases exhibit stronger optical absorption and higher charge separation efficiencies. Transient photocurrent analysis reveals a reduction of surface catalytic activity with increasing Cu:V elemental ratio due to competitive charge recombination at Cu-related surface states. This comprehensive analysis of PEC functionalities—including photon absorption, carrier separation, and heterogeneous charge transfer—informs strategies for improving PEC activity in the copper vanadate materials system and provides insights that may aid discovery, design, and engineering of new photoelectrode materials.

KEYWORDS: copper vanadate, photoelectrochemistry, photoanode, water oxidation, surface states, transient photocurrent analysis
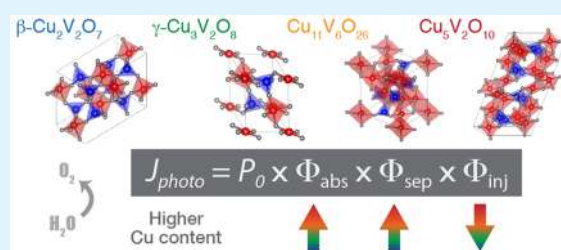
Various transition metal oxides have been explored as photoanodes for the light-driven oxygen evolution reaction (OER) because of their earth abundances, band energetics, and chemical stabilities.[1−5] Although a few semiconductors that possess these properties and have bandgaps suitable for harvesting solar photons have been identified,[6−10] experimentally obtained efficiencies tend to be significantly lower than theoretical limits. Indeed, incident photon-to-current efficiencies (IPCE) are often in the range of a few percent. Thus, identification of underlying loss mechanisms is an essential first step in determining the promise of newly discovered compounds and for devising strategies for increasing their efficiencies.

Ternary oxide systems provide a unique opportunity for tailoring material properties by varying metal combinations or stoichiometry.[11,12] For example, 15 ternary metal vanadates were recently identified as OER-active photoanodes.[2] The bandgaps (1.8−2.5 eV) and band edge characters of these materials are dictated by orbital hybridization between the VO_4-scaffold and the additional metal element. Among these materials, copper vanadate ($Cu_xV_yO_z$, hereafter referred to as CVO) is especially attractive since it is photochemically stable under mildly alkaline aqueous conditions and possesses <2 eV bandgaps. Several room-temperature stable phases with different Cu:V ratios exist, and moderate light-driven OER activities have been separately reported for different phases.[13−16] Herein, we perform a systematic analysis to determine whether correlations exist between the elemental composition and PEC functionalities. By analyzing trends in light absorption, charge separation, and surface recombination, we seek to elucidate the roles of constituent elements in CVO photoelectrodes, with a goal of identifying key loss mechanisms and potential strategies to address them. Additionally, comparing different phases within a specific material class provides insights that could qualitatively inform future metal oxide material discovery efforts in the field of PEC solar fuel production.

In general, the ability of a photoanode to convert incident irradiance, P_0, to photocurrent density, J_{photo}, can be quantitatively analyzed by the following formula:[17]

$$J_{photo} = P_0 \Phi_{abs} \Phi_{sep} \Phi_{inj} \tag{1}$$

where Φ_{abs} is the photon absorption probability, Φ_{sep} is the charge separation efficiency governed by the thickness of space charge layer and the minority carrier diffusion length, and Φ_{inj} is the charge injection efficiency denoting the yield of heterogeneous charge transfer across the semiconductor-liquid junction (SCLJ). In the presence of sacrificial reagents (e.g., H_2O_2 and Na_2SO_3), the interfacial hole transfer process is rapid and Φ_{inj} is often assumed to be near unity. However, we note
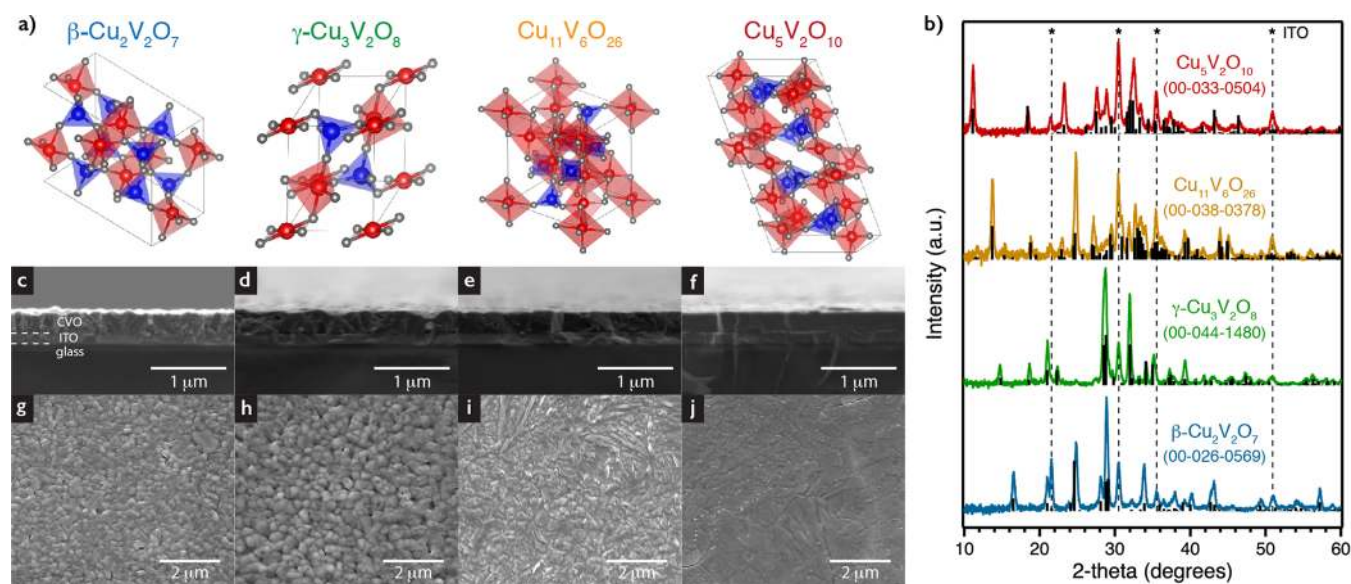
Figure 1. (a) Stoichiometry and crystal structures of the four CVO phases studied in this work. The Cu, V, and O atoms are labeled in red, blue, and gray, respectively. The black lines indicate the boundaries of each unit cell. (b) GIXRD patterns of four CVO thin films. Reference XRD stick spectra are shown as black lines. (c−f) Cross-sectional view and (g−j) plan-view SEM images of the four phases of CVO thin films grown on ITO substrates.

Table 1. Stoichiometries, optical bandgaps, and photoelectrochemical characteristics of the four CVO phases studied in this work

	[Cu]/([Cu]+ [V])			sulfite oxidation		water oxidation	
phase	expected	measured	bandgap (eV)	E_{on} (V)[a]	$J_{1.23}$ (mA/cm^2)[b]	E_{on} (V)[a]	$J_{1.23}$ (mA/cm^2)[b]
β-Cu$_2$V$_2$O$_7$	0.500	0.519	1.95	0.79	0.051	1.00	0.036
γ-Cu$_3$V$_2$O$_8$	0.600	0.621	1.95	0.78	0.105	0.94	0.071
Cu$_{11}$V$_6$O$_{26}$	0.647	0.655	1.83	0.73	0.125	0.94	0.053
Cu$_5$V$_2$O$_{10}$	0.714	0.725	2.03	0.67	0.206	1.34	0.001

[a]Photocurrent onset potential vs RHE scale, determined by linear extrapolation of the photocurrent onset of each J−E curve to zero current.
[b]Photocurrent density measured at 1.23 V vs RHE.

that it has recently been shown that the presence of a sacrificial reagent does not necessarily eliminate surface recombination losses. Thus, this assumption is not always correct and measurements with sacrificial reagents provide an lower limit to Φ_{sep}.[18] In the absence of sacrificial reagents, significant competition between the sluggish OER and surface recombination, as well as Fermi level pinning, is typical.[19] The accumulation of photogenerated holes and chemical transformations at the SCLJ can form additional surface states within the bandgap, which further reduces the photovoltage and opens new recombination pathways. In metal oxide photoanodes, such as α-Fe$_2$O$_3$ and BiVO$_4$, these surface states participate in water oxidation as reaction intermediates but also facilitate electron−hole recombination.[20−23] Accordingly, the overall OER kinetics depends on the dynamic balance between hole transfer (k_{CT}) and charge recombination (k_{rec}) rate constants. Taken together, the events governing overall photon-to-current conversion efficiency in eq 1 occur over a broad range of time scales and are affected by a variety of material properties that can be difficult to disentangle in a single compound.

In this work, morphologically compact thin films of four CVO compounds—β-Cu$_2$V$_2$O$_7$, γ-Cu$_3$V$_2$O$_8$, Cu$_{11}$V$_6$O$_{26}$, and Cu$_5$V$_2$O$_{10}$—were deposited onto ITO substrates by reactive co-sputtering (see the Supporting Information for experimental details). Although geometric Cu coordination varies between phases, the tetrahedrally coordinated VO$_4$ is a common motif (Figure 1a). The grazing incidence X-ray diffraction (GIXRD)

patterns lacked secondary peaks, thus indicating high phase purities (Figure 1b). The transition metal compositions, analyzed by ICP-MS and listed in Table 1, were within 2% of the stoichiometric values for each phase. XPS binding energies confirmed the dominant metal oxidation states to be Cu^{2+} and V^{5+}, and elemental Cu:V ratios at the surface resembled the bulk values (Figure S1). As shown by the cross-sectional SEM images in Figure 1c−f, every CVO film was grown to a thickness of 300 ± 10 nm to enable direct comparisons between the phases. The plan-view SEM images in Figure 1g−j revealed high coverage over large areas but with some differences in grain size. The β-Cu$_2$V$_2$O$_7$ thin film comprised grains of ∼100 nm diameter, whereas larger grains (150−300 nm) were observed in γ-Cu$_3$V$_2$O$_8$. In comparison, the two CVO phases with highest Cu:V ratios exhibited the most continuous morphologies. Importantly, the excellent homogeneity and low surface roughness of all of these films minimize light scattering and provide a platform suitable for baseline PEC performance evaluation.

PEC measurements of CVO photoanodes were conducted in 0.1 M sodium borate (NaB$_i$) buffer (pH 9.3) with an AM 1.5 solar simulator at 100 mW/cm^2 intensity. Figure 2 compares the current density versus applied electrochemical potential (J−E) responses under chopped illumination. In complementary measurements, the differences of measured J−E curves between dark and continuously illuminated conditions (Figure S3) were used to calculate photocurrent densities and the results are
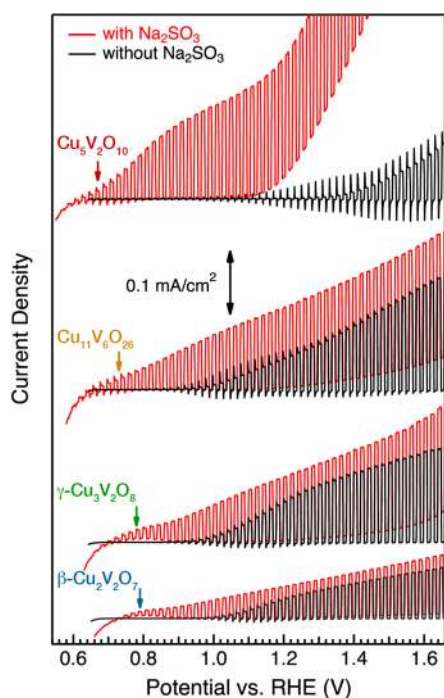
Figure 2. $J-E$ responses of 300 nm thick CVO thin films under front-side chopped AM 1.5 illumination at 100 mW/cm^2 in 0.1 M NaB$_i$ buffer (pH 9.3) with (red) and without (black) 0.1 M Na$_2$SO$_3$ added as sacrificial hole acceptor. Down-pointing arrows indicate the onsets of sulfite oxidation photocurrents obtained from continuous illumination experiments (Figure S4). The anodic polarization scan rate was 20 mV/s. Vertical offsets are applied to the data for ease of comparison.

summarized in Figure S4 and Table 1. When 0.1 M Na$_2$SO$_3$ was present as a sacrificial hole acceptor, the anodic photocurrent onset potentials occurred at applied potentials between 0.6−0.8 V vs RHE. As the Cu:V ratio increased, not only did the onset potential shift negatively from β-Cu$_2$V$_2$O$_7$ (0.79 V vs RHE) to Cu$_5$V$_2$O$_{10}$ (0.67 V vs RHE), the sulfite oxidation photocurrent increased with a greater slope beyond the onset region and reached a higher saturated current density. At 1.23 V vs RHE, Cu$_5$V$_2$O$_{10}$ exhibited a photocurrent density of 206 μA/cm^2, four times higher than the value of 51 μA/cm^2 obtained from β-Cu$_2$V$_2$O$_7$. The enhancement of sulfite oxidation photocurrent indicates more photogenerated holes were harvested at the SCLJ, and either the photon absorption efficiency Φ_{abs} or the charge separation efficiency Φ_{sep} (or both) was improved in Cu-rich CVO photoanodes. Meanwhile, notable dark currents, the origins of which are currently under investigation, emerged beyond 1.15 V vs RHE and became more pronounced in CVO phases with higher Cu contents. Because all samples had high coverage and the Cu-rich phases were particularly continuous, the observed dark current was unlikely to stem from exposed ITO substrate. Nonetheless, these background currents did not interfere with PEC characterization over a broad potential range since photocurrent onsets occurred at significantly more cathodic potentials.

In the absence of Na$_2$SO$_3$, the dark currents remained negligible over the entire 0.64−1.66 V vs RHE potential range. Under continuous illumination, the onset of photocurrent appeared at ∼1.35 V vs RHE for Cu$_5$V$_2$O$_{10}$ and ∼1 V vs RHE for other CVO phases (Figure S4). The water oxidation

photocurrent increased from β-Cu$_2$V$_2$O$_7$ to γ-Cu$_3$V$_2$O$_8$ and the slope of the $J-E$ profile exhibited positive curvature. In comparison, the photocurrent density of Cu$_{11}$V$_6$O$_{26}$ exhibited a slow and linear growth with potential and did not surpass that of γ-Cu$_3$V$_2$O$_8$ until applied potentials higher than 1.45 V vs RHE. The γ-Cu$_3$V$_2$O$_8$ and Cu$_{11}$V$_6$O$_{26}$ photoanodes remained stable under continuous illumination at 1.23 V vs RHE for at least 3 h, while β-Cu$_2$V$_2$O$_7$ showed ∼20% decay in photocurrent density during the same period (Figure S5). For Cu$_5$V$_2$O$_{10}$, the water oxidation photocurrent was negligible below 1.34 V vs RHE. Meanwhile, surface recombination caused photocurrent spikes near the onset regions under chopped illumination, and this effect was significantly more pronounced in Cu$_{11}$V$_6$O$_{26}$ and Cu$_5$V$_2$O$_{10}$ (Figure 2). The significantly reduced OER activity and severely increased surface recombination observed in Cu-rich phases implies that electronically active surface states are associated with Cu cations at the photoanode surface. Even though increasing Cu:V ratio resulted in higher photocurrents when Na$_2$SO$_3$ is present, Φ_{inj} was also considerably reduced. Understanding this apparent competition between bulk photocurrent generation and surface OER activity requires careful consideration of each factor in eq 1 as a function of CVO phase, as described below.

To clarify the separate roles of Φ_{abs} and Φ_{sep}, variable angle spectroscopic ellipsometry was used to determine optical properties of each investigated film and the absorption coefficients, $\alpha(\lambda)$, are shown in Figure 3a. The weak absorption peak ($\alpha < 1 \times 10^4$ cm^{-1}) between 700−1100 nm arises from localized ligand field excitation at the Cu^{2+} ($3d^9$) cations, and thus does not generate mobile charge carriers.[24] Tauc analysis assigned the optical bandgaps of these CVO compounds as indirect allowed transitions with similar magnitudes in the range of 1.83−2.03 eV (Figure S2), although $\alpha(\lambda)$ followed the
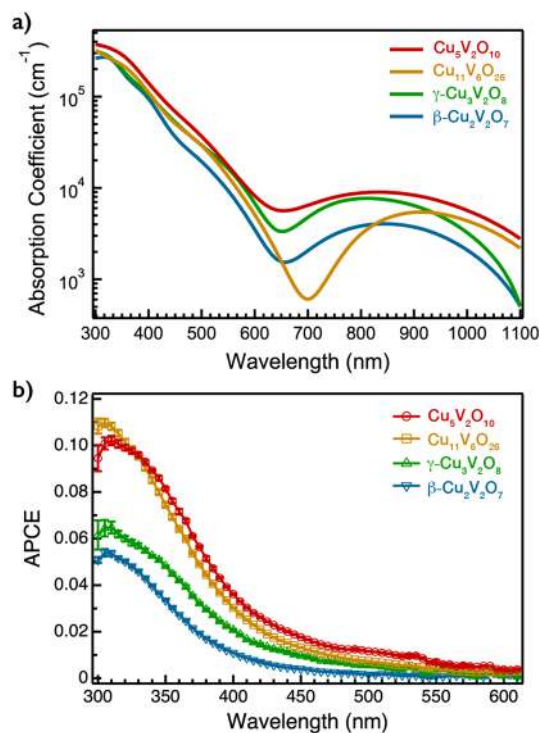

Figure 3. (a) Absorption coefficients for each CVO thin film as a function of wavelength. (b) APCE spectra collected at 1.23 V vs RHE in 0.1 M NaB$_i$ buffer with 0.1 M Na$_2$SO$_3$.
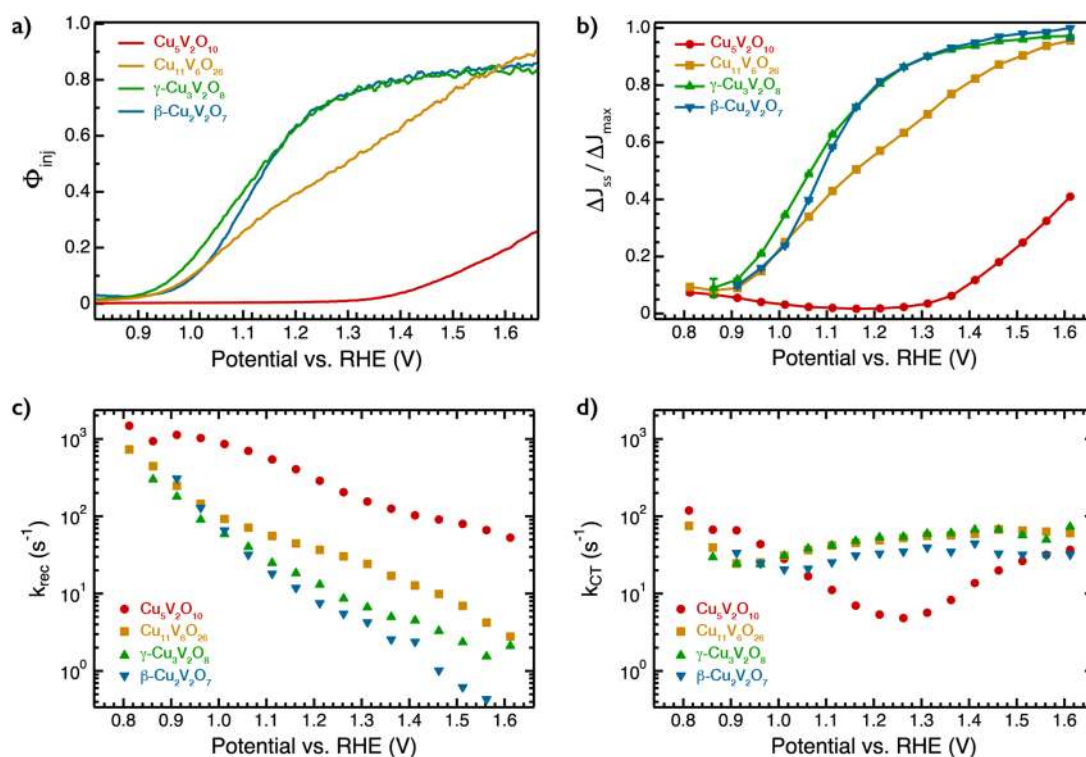
Figure 4. (a) Charge injection efficiencies, Φ_{inj}, determined from the ratio between sulfite oxidation photocurrent and water oxidation photocurrent for the four CVO phases. (b) Ratio between the steady state photocurrent ΔJ_{ss} and the instantaneous photocurrent ΔJ_{max} as a function of applied potential. (c) Surface electron−hole recombination rate constant, k_{rec}, as a function of applied potential. (d) Rate constant for heterogeneous hole transfer from the surface states to perform water oxidation, k_{CT}, as a function of applied potential.

trend of β-$Cu_2V_2O_7$ < γ-$Cu_3V_2O_8$ ≈ $Cu_{11}V_6O_{26}$ < $Cu_5V_2O_{10}$ in the above-bandgap region (300−650 nm). According to our previous spectroscopic study,[24] the bandgap of γ-$Cu_3V_2O_8$ corresponds to dominant $O(2p) \rightarrow Cu(3d)$ charge-transfer excitations. Therefore, the increasing absorption coefficients with respect to increasing Cu:V ratio could be linked to a higher partial density of Cu states at the conduction band minimum that manifest greater optical transition probabilities.

To quantify the charge separation efficiency, absorbed photon-to-current efficiencies (APCE; Figure 3b) were calculated at 1.23 V vs RHE for the facile sulfite oxidation reaction by dividing the IPCE (Figure S6) spectra with the corresponding absorbance spectra. All CVO thin films exhibited similar APCE profiles, with onset of detectable photocurrent at ~570 nm. Nevertheless, Cu-rich phases still demonstrated higher hole collection efficiencies, indicating that increasing Cu content also improves charge separation in CVO. While intrinsic electronic structure trends, such as higher degrees of $Cu(3d)$−$O(2p)$ hybridization with increasing Cu:V ratios, may serve to improve hole mobility, additional research into the fundamental character of charge carriers (i.e., hole polarons and their associated properties[25]) and point defect contributions to transport (i.e., trapping, recombination, and doping) will be required to elucidate the mechanisms underlying the empirically observed trend in charge separation efficiency. Nevertheless, these results indicate that both Φ_{abs} and Φ_{sep} increase with increasing Cu:V ratio.

The charge injection efficiency, Φ_{inj}, was determined for each CVO photoanode by the ratio between water and sulfite oxidation photocurrents (Figure 4a). Despite the fact that γ-$Cu_3V_2O_8$ generates a two times larger sulfite oxidation photocurrent than β-$Cu_2V_2O_7$, both compounds possess similar

profiles of Φ_{inj}; the charge injection efficiency increased rapidly following the onset potential and plateaued at a value of ~0.8 starting at ~1.3 V vs RHE. Because depletion of electrons from the surface at high applied potentials suppresses surface recombination, the less-than-unity Φ_{inj} in this range does not reflect the competition between heterogeneous charge transfer (k_{CT}) and charge recombination (k_{rec}) in the same way that it does near the onset. Rather, the extra potential required to compensate for Fermi level pinning shifts the J−E curve anodically in the absence of sacrificial reagent. In Figure S4, this horizontal offset can be estimated to be ~140 and 180 mV for β-$Cu_2V_2O_7$ and γ-$Cu_3V_2O_8$, respectively. For the case of $Cu_{11}V_6O_{26}$, Φ_{inj} also reached a value of ~0.8 level at highly anodic potentials but its value was significantly lower at moderate bias (1.1−1.4 V vs RHE) than for β-$Cu_2V_2O_7$ and γ-$Cu_3V_2O_8$. Although $Cu_5V_2O_{10}$ exhibited the best PEC characteristics for sulfite oxidation among four CVO phases, its much lower OER catalytic activity arose from a much lower Φ_{inj}, which barely reached 0.2 at 1.66 V vs RHE. Coupled with the previously discussed photocurrent spikes under chopped illumination (Figure 2), we suggest that Cu-related surface states facilitated electron−hole recombination and caused the decreasing trend of charge injection efficiency, Φ_{inj}, with increasing Cu:V ratio in CVO photoanodes. While OER mechanism involves surface peroxo or superoxo species[26] on TiO_2 photoanode, Fe^{IV}=O surface intermediate[27] is observed on α-Fe_2O_3 by operando infrared spectroscopy. Therefore, considering the d-orbital occupancies, it is reasonable for Cu^{2+} ($3d^9$), instead of V^{5+} ($3d^0$), to form highly oxidized surface states on CVO photoanodes during light-driven OER.

The kinetics associated with photogenerated holes at the SCLJ was studied by transient photocurrent analysis using a

pulsed 340 nm LED and a continuous white light source. The same technique has been applied to quantify the kinetics of accumulated holes on the α-Fe$_2$O$_3$ surface.[28] The transient photocurrent responses of the four different CVO photoanodes were collected in 0.1 M NaB$_i$ buffer between 0.8−1.6 V vs RHE (Figure S7). Such photocurrent spikes were only observed at low to moderate potentials, with the exception of Cu$_5$V$_2$O$_{10}$, which exhibited significant surface recombination over the entire potential range. For each current−time trace in Figure S7, an exponential fit was performed based on the data analysis scheme depicted in Figure S8. Here, J_0 denotes the photocurrent density generated by the continuous background illumination, J_{max} describes the instantaneous photocurrent when the 340 nm LED is turned on, and J_{ss} is the newly reached steady state photocurrent. The branching probability for heterogeneous hole transfer at the surface states is given by the following formula:[20]

$$\frac{\Delta J_{ss}}{\Delta J_{max}} = \frac{J_{ss} - J_0}{J_{max} - J_0} = \frac{k_{CT}}{k_{CT} + k_{rec}} \quad (2)$$

In addition, the decay time constant of the photocurrent spike correlates to the sum of charge transfer (k_{CT}) and recombination (k_{rec}) rate constants:[20]

$$\frac{J(t) - J_{ss}}{J_{max} - J_{ss}} = e^{-(k_{CT} + k_{rec})t} \quad (3)$$

Figure S9 plots the background photocurrents, J_0, as a function of applied potential, and for every CVO compound the results matched the water oxidation $J−E$ characteristics in Figure S4. More importantly, the 340 nm pulses provided merely 5−7% perturbation to J_0, implying the hole quasi-Fermi level was not shifted notably by the modulating light source. Accordingly, k_{CT} and k_{rec} obtained from this analysis using eqs 2 and 3 are representative of the 1 sun operating condition.

The plots of $\Delta J_{ss}/\Delta J_{max}$ and photocurrent spike decay times for each CVO photoanode are shown in Figure 4b and Figure S10, respectively. Resemblances can be drawn between the $\Delta J_{ss}/\Delta J_{max}$ plots, obtained by transient photocurrent analysis in the absence of sacrificial reagents at fixed potentials, and the Φ_{inj} profiles in Figure 4a, which were calculated from steady state linear sweep voltammetry data for water and sulfite oxidations. However, while Φ_{inj} saturated at ∼0.8 because of Fermi level pinning, $\Delta J_{ss}/\Delta J_{max}$ reached a near-unity plateau at higher applied potentials. The values of k_{rec} and k_{CT} obtained by solving eqs 2 and 3 are presented as a function of applied potential in Figure 4c, d, respectively. The rate constants that ranged between 1−100 s^{-1} are similar to the values measured on α-Fe$_2$O$_3$ using photoelectrochemical impedance techniques.[29,30] For each CVO compound, the logarithm of k_{rec} exhibits a monotonic decline with increasing applied potential (Figure 4c), which can be explained by the reduced surface electron concentration, n_e^{surf}, arising from increased band bending ($\Delta\phi_{sc}$) at the SCLJ:

$$k_{rec} = \sigma_p \nu_{th} n_e^{surf} \propto \sigma_p \nu_{th} \exp\left(\frac{-q\Delta\phi_{sc}}{k_B T}\right) \quad (4)$$

in which σ_p is the electron capture cross-section of holes, and ν_{th} is the electron thermal velocity. In samples with higher Cu:V ratios, surface recombination occurred faster and was less likely to be mitigated by increasing applied potential. This trend is consistent with the hypothesis that the surface states are formed

around the Cu sites, such that a higher surface state density increases the recombination rate and pins the surface Fermi level. In contrast to k_{rec}, the heterogeneous charge transfer rate constant k_{CT} remains relatively constant in the range of 20−50 s^{-1} for all applied biases (Figure 4d), with a 2-fold increase of k_{CT} observed between 1.0−1.3 V vs RHE for β-Cu$_2$V$_2$O$_7$, γ-Cu$_3$V$_2$O$_8$, and Cu$_{11}$V$_6$O$_{26}$. Importantly, within this potential range, the decrease of k_{rec} was less pronounced compared with lower and higher applied potential regions. This correlation suggests that Fermi level pinning was most severe between 1.0−1.3 V vs RHE and that an additional voltage drop in the Helmholtz layer modified the OER barrier height and thus k_{CT}. Taken together, the competition between k_{rec} and k_{CT} determines the catalytic activity of a photoanode surface. Only at high applied potentials that are sufficient to mitigate surface recombination do charge transfer process become competitive and Faradaic OER photocurrents appear. In this respect, although Cu-rich CVO phases possess higher absorption coefficients and charge separation efficiencies, the presence of high concentrations of electronically active surface states results in poorer PEC performance than for phases with lower Cu:V ratios. These findings point to the necessity of passivating Cu-related surface states, as well as the opportunities for integrating cocatalysts onto Cu-rich phases that exhibit superior bulk properties for solar energy capture.

It is worth considering that the performance obtained from CVO is remarkably similar to other visible-light-absorbing oxides comprising transition metals with partially occupied d-orbitals, such as CuWO$_4$ and α-Fe$_2$O$_3$.[8,20] As has been previously suggested,[31] poor electronic transport in this class of highly correlated electron materials may be a significant hurdle to achieving high performance photoelectrodes. While nanostructuring to match physical dimensions to charge extraction lengths is a proven strategy for enhancing the performance of such systems and would be worth further exploration for the case of CVO, more suitable charge transport characteristics might be found among d^0 and d^{10} transition metal oxides. A prototypical example of such a material is BiVO$_4$,[32] which represents the highest performance visible light absorbing transition metal oxide. While its 2.5 eV bandgap[33] provides a rather low thermodynamic limit to photocurrent generation, state-of-the-art photoanodes achieve in >60% APCE.[7] By comparison, the low APCE (1−10%) of CVO thin films is indicative of a dramatic mismatch between the optical absorption depth and the charge extraction length, which is severely limited by the hole diffusion length, L_p, for all phases reported here.

In summary, four CVO phases—β-Cu$_2$V$_2$O$_7$, γ-Cu$_3$V$_2$O$_8$, Cu$_{11}$V$_6$O$_{26}$, and Cu$_5$V$_2$O$_{10}$—were prepared by reactive co-sputtering, and their PEC performance characteristics were systematically compared and analyzed. All four compounds possess indirect bandgaps in the range of 1.83−2.03 eV, and the imbalance between absorption length α^{-1} and hole diffusion length L_p places a critical limitation on their light harvesting efficiencies. The Cu-rich phases exhibit higher absorption coefficients, consistent with the O(2p) → Cu(3d) bandgap transition. In addition, the charge separation efficiencies measured by APCE also improve with increasing Cu:V ratio, though it is not yet clear whether the underlying cause is an intrinsic property arising from electronic structure trends in the material or is associated with extrinsic defect-related processes. Regardless, Fermi level pinning and formation of surface states correlated with Cu content were observed on every CVO

compound under OER conditions. While the heterogeneous charge transfer rate constants were similar for all phases, surface recombination was significantly more detrimental to the OER catalytic activity for Cu-rich compositions. The competing trends of bulk and surface properties with respect to elemental Cu:V ratio highlight the challenging task in optimizing PEC energy conversion efficiency in emerging ternary oxide semiconductors. Valuable insights provided by the CVO model system could help further design and optimization of new oxide-based photoelectrodes.

ASSOCIATED CONTENT

Ⓢ Supporting Information

The Supporting Information is available free of charge on the ACS Publications website at DOI: 10.1021/acsami.8b02977.

> Experimental details for thin film preparation and characterization; XPS data at valence band, Cu 2p, V 2p, and O 1s levels; plots of Tauc analyst; $J-E$ curves under continuous illumination in the presence of Na_2SO_3; results of chronoamperometric measurements; IPCE spectra; transient photocurrent responses; transient photocurrent analysis scheme (PDF)

AUTHOR INFORMATION

Corresponding Author
*E-mail: sharp@wsi.tum.de. Phone: +49-(0)89-289-11582. Fax: +49-(0)89-12737.

ORCID Ⓘ
Chang-Ming Jiang: 0000-0001-8327-5760
Ian D. Sharp: 0000-0001-5238-7487

Notes
The authors declare no competing financial interest.

REFERENCES

(1) Sivula, K.; van de Krol, R. Semiconducting Materials for Photoelectrochemical Energy Conversion. *Nat. Rev. Mater.* **2016**, *1*, 15010.

(2) Yan, Q.; Yu, J.; Suram, S. K.; Zhou, L.; Shinde, A.; Newhouse, P. F.; Chen, W.; Li, G.; Persson, K. A.; Gregoire, J. M.; et al. Solar Fuels Photoanode Materials Discovery by Integrating High-Throughput Theory and Experiment. *Proc. Natl. Acad. Sci. U. S. A.* **2017**, *114*, 3040−3043.

(3) Shinde, A.; Suram, S. K.; Yan, Q.; Zhou, L.; Singh, A. K.; Yu, J.; Persson, K. A.; Neaton, J. B.; Gregoire, J. M. Discovery of Manganese-Based Solar Fuel Photoanodes via Integration of Electronic Structure Calculations, Pourbaix Stability Modeling, and High-Throughput Experiments. *ACS Energy Lett.* **2017**, *2*, 2307−2312.

(4) Kudo, A.; Miseki, Y. Heterogeneous Photocatalyst Materials for Water Splitting. *Chem. Soc. Rev.* **2009**, *38*, 253−278.

(5) Hisatomi, T.; Kubota, J.; Domen, K. Recent Advances in Semiconductors for Photocatalytic and Photoelectrochemical Water Splitting. *Chem. Soc. Rev.* **2014**, *43*, 7520−7535.

(6) Kim, J. Y.; Magesh, G.; Youn, D. H.; Jang, J.-W.; Kubota, J.; Domen, K.; Lee, J. S. Single-Crystalline, Wormlike Hematite Photoanodes for Efficient Solar Water Splitting. *Sci. Rep.* **2013**, *3*, 2681.

(7) Kim, T. W.; Choi, K.-S. Nanoporous $BiVO_4$ Photoanodes with Dual-Layer Oxygen Evolution Catalysts for Solar Water Splitting. *Science* **2014**, *343*, 990−994.

(8) Lhermitte, C. R.; Bartlett, B. M. Advancing the Chemistry of $CuWO_4$ for Photoelectrochemical Water Oxidation. *Acc. Chem. Res.* **2016**, *49*, 1121−1129.

(9) Guo, Y.; Zhang, N.; Wang, X.; Qian, Q.; Zhang, S.; Li, Z.; Zou, Z. A Facile Spray Pyrolysis Method to Prepare Ti-Doped $ZnFe_2O_4$ for Boosting Photoelectrochemical Water Splitting. *J. Mater. Chem. A* **2017**, *5*, 7571−7577.

(10) Newhouse, P. F.; Reyes-Lillo, S. E.; Li, G.; Zhou, L.; Shinde, A.; Guevarra, D.; Suram, S. K.; Soedarmadji, E.; Richter, M. H.; Qu, X.; et al. Discovery and Characterization of a Pourbaix-Stable, 1.8 eV Direct Gap Bismuth Manganate Photoanode. *Chem. Mater.* **2017**, *29*, 10027−10036.

(11) Toroker, M. C.; Carter, E. A. Transition Metal Oxide Alloys as Potential Solar Energy Conversion Materials. *J. Mater. Chem. A* **2013**, *1*, 2474−2484.

(12) Guijarro, N.; Bornoz, P.; Prévot, M.; Yu, X.; Zhu, X.; Johnson, M.; Jeanbourquin, X.; Le Formal, F.; Sivula, K. Evaluating Spinel Ferrites MFe_2O_4 (M = Cu, Mg, Zn) as Photoanodes for Solar Water Oxidation: Prospects and Limitations. *Sustain Energy Fuels* **2018**, *2*, 103−117.

(13) Seabold, J. A.; Neale, N. R. All First Row Transition Metal Oxide Photoanode for Water Splitting Based on $Cu_3V_2O_8$. *Chem. Mater.* **2015**, *27*, 1005−1013.

(14) Guo, W.; Chemelewski, W. D.; Mabayoje, O.; Xiao, P.; Zhang, Y.; Mullins, C. B. Synthesis and Characterization of CuV_2O_6 and $Cu_2V_2O_7$: Two Photoanode Candidates for Photoelectrochemical Water Oxidation. *J. Phys. Chem. C* **2015**, *119*, 27220−27227.

(15) Zhou, L.; Yan, Q.; Shinde, A.; Guevarra, D.; Newhouse, P. F.; Becerra-Stasiewicz, N.; Chatman, S. M.; Haber, J. A.; Neaton, J. B.; Gregoire, J. M. High Throughput Discovery of Solar Fuels Photoanodes in the $CuO-V_2O_5$ System. *Adv. Energy Mater.* **2015**, *5*, 1500968.

(16) Lumley, M. A.; Choi, K.-S. Investigation of Pristine and (Mo, W)-Doped $Cu_{11}V_6O_{26}$ for Use as Photoanodes for Solar Water Splitting. *Chem. Mater.* **2017**, *29*, 9472−9479.

(17) Dotan, H.; Sivula, K.; Grätzel, M.; Rothschild, A.; Warren, S. C. Probing the Photoelectrochemical Properties of Hematite (α-Fe_2O_3) Electrodes Using Hydrogen Peroxide as a Hole Scavenger. *Energy Environ. Sci.* **2011**, *4*, 958−964.

(18) Segev, G.; Jiang, C.-M.; Cooper, J. K.; Eichhorn, J.; Toma, F. M.; Sharp, I. D. Quantification of the Loss Mechanisms in Emerging Water Splitting Photoanodes Through Empirical Extraction of the Spatial Charge Collection Efficiency. *Energy Environ. Sci.* **2018**, DOI: 10.1039/C7EE03486E.

(19) Sivula, K. Metal Oxide Photoelectrodes for Solar Fuel Production, Surface Traps, and Catalysis. *J. Phys. Chem. Lett.* **2013**, *4*, 1624−1633.

(20) Peter, L. M. Energetics and Kinetics of Light-Driven Oxygen Evolution at Semiconductor Electrodes: The Example of Hematite. *J. Solid State Electrochem.* **2013**, *17*, 315−326.

(21) Klahr, B.; Gimenez, S.; Fabregat-Santiago, F.; Hamann, T.; Bisquert, J. Water Oxidation at Hematite Photoelectrodes: The Role of Surface States. *J. Am. Chem. Soc.* **2012**, *134*, 4294−4302.

(22) Le Formal, F.; Pastor, E.; Tilley, S. D.; Mesa, C. A.; Pendlebury, S. R.; Gratzel, M.; Durrant, J. R. Rate Law Analysis of Water Oxidation on a Hematite Surface. *J. Am. Chem. Soc.* **2015**, *137*, 6629−6637.

(23) Ma, Y.; Mesa, C. A.; Pastor, E.; Kafizas, A.; Francàs, L.; Le Formal, F.; Pendlebury, S. R.; Durrant, J. R. Rate Law Analysis of Water Oxidation and Hole Scavenging on a $BiVO_4$ Photoanode. *ACS Energy Lett.* **2016**, *1*, 618−623.

(24) Jiang, C.-M.; Farmand, M.; Wu, C. H.; Liu, Y.-S.; Guo, J.; Drisdell, W. S.; Cooper, J. K.; Sharp, I. D. Electronic Structure, Optoelectronic Properties, and Photoelectrochemical Characteristics of γ-$Cu_3V_2O_8$ Thin Films. *Chem. Mater.* **2017**, *29*, 3334−3345.

(25) Lany, S. Semiconducting Transition Metal Oxides. *J. Phys.: Condens. Matter* **2015**, *27*, 283203.

(26) Nakamura, R.; Nakato, Y. Primary Intermediates of Oxygen Photoevolution Reaction on TiO_2 (Rutile) Particles, Revealed by in Situ FTIR Absorption and Photoluminescence Measurements. *J. Am. Chem. Soc.* **2004**, *126*, 1290−1298.

(27) Zandi, O.; Hamann, T. W. Determination of Photoelectrochemical Water Oxidation Intermediates on Haematite Electrode Surfaces Using Operando Infrared Spectroscopy. *Nat. Chem.* **2016**, *8*, 778−783.

(28) Le Formal, F.; Sivula, K.; Grätzel, M. The Transient Photocurrent and Photovoltage Behavior of a Hematite Photoanode under Working Conditions and the Influence of Surface Treatments. *J. Phys. Chem. C* **2012**, *116*, 26707−26720.

(29) Upul Wijayantha, K. G.; Saremi-Yarahmadi, S.; Peter, L. M. Kinetics of Oxygen Evolution at α-Fe_2O_3 Photoanodes: A Study by Photoelectrochemical Impedance Spectroscopy. *Phys. Chem. Chem. Phys.* **2011**, *13*, 5264−5270.

(30) Peter, L. M.; Wijayantha, K. G. U.; Tahir, A. A. Kinetics of Light-Driven Oxygen Evolution at α-Fe_2O_3 Electrodes. *Faraday Discuss.* **2012**, *155*, 309−322.

(31) Huda, M. N.; Al-Jassim, M. M.; Turner, J. A. Mott Insulators: An Early Selection Criterion for Materials for Photoelectrochemical H_2 Production. *J. Renewable Sustainable Energy* **2011**, *3*, 053101.

(32) Cooper, J. K.; Gul, S.; Toma, F. M.; Chen, L.; Glans, P.-A.; Guo, J.; Ager, J. W.; Yano, J.; Sharp, I. D. Electronic Structure of Monoclinic $BiVO_4$. *Chem. Mater.* **2014**, *26*, 5365−5373.

(33) Cooper, J. K.; Gul, S.; Toma, F. M.; Chen, L.; Liu, Y.-S.; Guo, J.; Ager, J. W.; Yano, J.; Sharp, I. D. Indirect Bandgap and Optical Properties of Monoclinic Bismuth Vanadate. *J. Phys. Chem. C* **2015**, *119*, 2969−2974.